Journal of High Energy Astrophysics 37 (2023) 51–61

Contents lists available at ScienceDirect

Journal of High Energy Astrophysics

journal homepage: www.elsevier.com/locate/jheap

Synchrotron self-compton emission in the two-component jet model for gamma-ray bursts

Yuri Sato [a,*], Kaori Obayashi [a], B. Theodre Zhang [b], Shuta J. Tanaka [a,c], Kohta Murase [d,e,f,b], Yutaka Ohira [g], Ryo Yamazaki [a,h]

[a] Department of Physical Sciences, Aoyama Gakuin University, 5-10-1 Fuchinobe, Sagamihara, Kanagawa 252-5258, Japan
[b] Center for Gravitational Physics, Yukawa Institute for Theoretical Physics, Kyoto, Kyoto 606-8502, Japan
[c] Graduate School of Engineering, Osaka University, 2-1 Yamadaoka, Suita, Osaka 565-0871, Japan
[d] Department of Physics, The Pennsylvania State University, University Park, PA 16802, USA
[e] Department of Astronomy and Astrophysics, The Pennsylvania State University, University Park, PA 16802, USA
[f] Center for Multimessenger Astrophysics, Institute for Gravitation and the Cosmos, The Pennsylvania State University, University Park, PA 16802, USA
[g] Department of Earth and Planetary Science, The University of Tokyo, 7-3-1 Hongo, Bunkyo-ku, Tokyo 113-0033, Japan
[h] Institute of Laser Engineering, Osaka University, 2-6, Yamadaoka, Suita, Osaka 565-0871, Japan

ARTICLE INFO

Article history:
Received 2 September 2022
Received in revised form 27 October 2022
Accepted 17 December 2022

Keywords:
Gamma-ray bursts: general

ABSTRACT

Gamma-ray bursts (GRBs) are intense bursts of high-energy photons (prompt emissions) caused by relativistic jets. After the emissions, multi-wavelength afterglows, from radio to very-high-energy (VHE) gamma-ray, last for more than a few days. In the past three years, the VHE gamma-ray photons from four GRBs (GRBs 180720B, 190114C, 190829A and 201216C) were detected by ground-based Imaging Atmospheric Cherenkov Telescopes, such as the Major Atmospheric Gamma Imaging Cherenkov (MAGIC) telescopes and the High Energy Stereoscopic System (H.E.S.S.). One of them, GRB 190829A, had some peculiar features of showing achromatic peaks in X-ray and optical bands at 1.4×10^3 s and being classified as low-luminosity GRBs. Previously, we proposed a two-component jet model, which has 'narrow jet' with a small initial opening half-angle $\theta_0 = 0.015$ rad and large bulk Lorentz factor $\Gamma_0 = 350$, and 'wide jet' with $\theta_0 = 0.1$ rad and $\Gamma_0 = 20$. The narrow jet explained the early X-ray and optical emissions and apparently small isotropic gamma-ray energy and peak energy in the off-axis viewing case. Furthermore, the late X-ray and radio (1.3 and 15.5 GHz) afterglows were emitted from the wide jet. Here, we calculate the VHE gamma-ray flux by the synchrotron self-Compton (SSC) emission. The multi-wavelength afterglows of GRB 190829A including the VHE gamma-ray emission are well explained by our two-component jet model. The afterglow emissions from our two-component jet are also consistent with the observational results of GRBs 180720B, 190114C and 201216C, when the jets are viewed on-axis. Furthermore, we discuss the detectability of off-axis orphan afterglows by the Cherenkov Telescope Array (CTA).

1. Introduction

Gamma-ray bursts (GRBs) are intense bursts of high-energy (between 10 keV and 10 MeV) photons (prompt emissions), and the duration of the emission ranges between 0.1 and 1000 seconds (Piran, 2004). After the prompt emission, multi-wavelength afterglows, from radio to very-high-energy (VHE) gamma-rays, last for more than a few days (Mészáros and Rees, 1997). It is believed that gamma-ray photons are emitted by relativistic jets toward us (fireball model) (Piran, 1999; Pe'er, 2015). The jet is slowed down by the interaction with the ambient interstellar matter (ISM), and subsequently the external shock is formed (Meszaros and Rees, 1993). Currently, the details of the prompt radiation mechanisms and the central engine have not been well understood.

In the past three years, the VHE gamma-ray photons from four GRBs, GRB 180720B (Abdalla et al., 2019), GRB 190114C (MAGIC Collaboration, 2019a), GRB 190829A (H.E.S.S. Collaboration, 2021) and GRB 201216C (Blanch et al., 2020b), were detected by ground-based Imaging Atmospheric Cherenkov Telescopes, such as the Major Atmospheric Gamma Imaging Cherenkov (MAGIC) telescopes

* Corresponding author.
E-mail address: yuris@phys.aoyama.ac.jp (Y. Sato).

https://doi.org/10.1016/j.jheap.2022.12.004
2214-4048/

and the High Energy Stereoscopic System (H.E.S.S.). Furthermore, MAGIC has reported the VHE gamma-ray photons with $\sim 3\sigma$ significance from GRBs 160821B (Acciari et al., 2021) and 201015A (Blanch et al., 2020a).

The VHE gamma-ray flux from GRB 190829A was detected by H.E.S.S. with 0.2–4.0 TeV energy flux of $\sim 4.0 \times 10^{-11}$ erg s^{-1} cm^{-2} at $t \sim 2 \times 10^4$ s after the burst onset (H.E.S.S. Collaboration, 2021). This event had much smaller isotropic-equivalent luminosity, $L_{\rm iso} = 10^{49}$ erg s^{-1}, than typical long GRBs, and was classified as low-luminosity GRBs (Chand et al., 2020). The prompt emission of GRB 190829A consists of two episodes (Chand et al., 2020). According to Chand et al. (2020), the first emission (Episode 1) had the isotropic gamma-ray energy $E_{\rm iso,\gamma} = 3.2 \times 10^{49}$ erg and the peak photon energy of the νF_ν spectrum $E_p = 120.0$ keV. At about 40 s after Episode 1, the second brighter emission with $E_{\rm iso,\gamma} = 1.9 \times 10^{50}$ erg and $E_p = 10.9$ keV was observed (Episode 2). The values of $E_{\rm iso,\gamma}$ and E_p of both Episodes 1 and 2 were smaller than typical long GRBs (Chand et al., 2020). GRB 190829A was located at a low redshift $z = 0.0785$ (Valeev et al., 2019). The very long baseline interferometry (VLBI) observations gave the upper limits on the source size in the radio bands (Salafia et al., 2022). Furthermore, the 3σ upper limit on the optical linear polarization of $\lesssim 6\%$ was also observed at $t \sim 3.0 \times 10^3$ s (Dichiara et al., 2022). It was associated with a type-Ic supernova SN 20190yw (Hu et al., 2021).

The multi-wavelength afterglows of GRB 190829A, were obtained in the VHE gamma-ray (H.E.S.S. Collaboration, 2021), X-ray, optical/infrared (IR) (Chand et al., 2020) and radio bands (Rhodes et al., 2020; Salafia et al., 2022; Dichiara et al., 2022). The X-ray and optical light curves had achromatic peaks at 1.4×10^3 s (Chand et al., 2020). It is difficult for the standard afterglow model to explain such achromatic peaks (Sari et al., 1998), so that the X-ray flare model (Chand et al., 2020; Zhang et al., 2021b), the baryon loaded outflow model (Fraija et al., 2021), the e^+e^- dust shell model (Zhang et al., 2021a) and the reverse-shock emission model (Salafia et al., 2022; Dichiara et al., 2022) have been proposed. We proposed an off-axis two-component jet model in order to explain small values of $E_{\rm iso,\gamma}$ and E_p, and simultaneous afterglow peaks in X-ray and optical bands (Sato et al., 2021).

The VHE gamma-ray afterglows from bright GRBs 180720B and 190114C could be explained by the synchrotron self-Compton (SSC) mechanism (e.g. Derishev and Piran, 2019; Fraija et al., 2019a,b,c; MAGIC Collaboration, 2019b; Asano et al., 2020; Huang et al., 2021; Derishev and Piran, 2021; Yamasaki and Piran, 2022) and/or the photohadronic model (Sahu and Fortín, 2020). For GRB 190829A, the external inverse-Compton (Zhang et al., 2021b) and photohadronic (Sahu et al., 2022) models have been proposed in addition to the SSC emission model.

It was shown in Sato et al. (2021) that the observational results of GRB 190829A were consistent with the off-axis two-component jet model which consists of two uniform jets ('narrow' and 'wide' jets). The early X-ray and optical light curves of GRB 190829A could be off-axis emissions from the narrow jet with initial opening half-angle $\theta_0 = 0.015$ rad and initial bulk Lorentz factor $\Gamma_0 = 350$. The wide jet, which has $\theta_0 = 0.1$ rad and $\Gamma_0 = 20$, explained the late X-ray and radio (1.3 and 15.5 GHz) afterglows. The hydrodynamic simulation showed that GRB jets are structured with an angular dependent energy distribution (e.g. Zhang and MacFadyen, 2009; Gottlieb et al., 2020; Urrutia et al., 2022). The two-component jet may be the most simple approximation of 'the structured-jets' with envelopes. Sato et al. (2021) did not calculate the VHE gamma-ray afterglows of GRB 190829A. In this paper, we discuss our off-axis two-component jet model to explain multi-wavelength afterglows including the VHE gamma-ray flux for GRB 190829A. In the present study, we calculate the SSC flux, using the jet parameters similar to those determined by Sato et al. (2021). The radio emissions in 5.5 and 99.8 GHz are also computed to explain the observed ones.

Furthermore, we discuss whether our two-component jet model could explain the observational results of the other VHE gamma-ray events (GRBs 180720B, 190114C and 201216C). GRB 190829A had the achromatic peaks $t \sim 1.4 \times 10^3$ s and the small value of $E_{\rm iso,\gamma}$ and E_p (Chand et al., 2020), while GRBs 180720B, 190114C and 201216C showed monotonically decaying X-ray light curve (Fraija et al., 2019b; Yamazaki et al., 2020) and had typical isotropic equivalent gamma-ray energy and peak energy (GRB 180720B: $E_{\rm iso,\gamma} = 6.0 \times 10^{53}$ erg (Abdalla et al., 2019) and $E_p = 631$ keV (Duan and Wang, 2019), GRB 190114C: $E_{\rm iso,\gamma} = 2.5 \times 10^{53}$ erg (MAGIC Collaboration, 2019b) and $E_p = 998.6$ keV (Ravasio et al., 2019) and GRB 201216C: $E_{\rm iso,\gamma} = 4.7 \times 10^{53}$ erg (Blanch et al., 2020a) and $E_p = 326$ keV (Huang, 2022)). We explained the observational results of GRB 190829A by our off-axis two-component jet model (thick red solid arrow in Fig. 1) (Sato et al., 2021). The other three VHE gamma-ray events have been considered that the jets are explained as on-axis emissions (e.g. Wang et al., 2019; MAGIC Collaboration, 2019a; Asano et al., 2020; Huang, 2022; Rhodes et al., 2022). In this paper, we calculate the afterglow emissions for GRBs 180720B, 190114C and 201216C in the on-axis viewing case following previous works (thin blue solid arrow in Fig. 1).

The afterglows which are not associated with the prompt emission are called 'orphan afterglows' (Piran, 2004). The gravitational lensing effect model (Gao et al., 2022), the dirty fireball model (Ho et al., 2022) and the off-axis afterglow model (e.g. Nakar et al., 2002; Totani and Panaitescu, 2002; Urata et al., 2015) have been proposed for the origin of orphan afterglows. Orphan afterglows have not yet been definitively detected (e.g. Zhang, 2018; Ho et al., 2020, 2022; Huang et al., 2020). In this paper, we discuss prospects of detecting of off-axis orphan afterglows by the Large-Sized Telescope (LST) of the Cherenkov Telescope Array (CTA) (thin green dashed arrow in Fig. 1). Owing to a large field of view of CTA/LST (Cherenkov Telescope Array Consortium et al., 2019), it may have high detectability of orphan afterglows. The detection of orphan afterglow by CTA/LST may indicate the existence of the wide jet with the low Lorentz factor introduced in our model. We also discuss the detectability of multi-wavelength orphan afterglows by the extended Roentgen Survey with an Imaging Telescope Array (eROSITA), the Vera C. Rubin Legacy Survey of Space and Time (Rubin LSST), the Zwicky Transient Facility (ZTF), the Atacama Large Millimeter/sub-millimeter Array (ALMA), the next generation Very Large Array (ngVLA) and the Square Kilometre Array (SKA).

In § 2, our numerical method is explained. In Sato et al. (2021), the number fraction of accelerated electrons f_e was fixed to unity, and only the Thomson limit was considered in calculating the cooling frequency and SSC flux. In this paper, we calculate the SSC emission taking into account the Klein-Nishina effect, and changing the number fraction of accelerated electrons f_e. In § 3.1, we show our results of the multi-wavelength afterglow emissions for GRB 190829A. In § 3.2, we use our two-component jet model determined in § 3.1 to explain the multi-wavelength light curves of GRBs 180720B, 190114C and 201216C. If our model with the narrow jet with large Γ_0 and the wide jet with small Γ_0 is suitable for VHE gamma-ray events, orphan afterglow emissions from the wide jet viewed off-axis may be observed. In § 3.3, we show the detectability of off-axis orphan afterglow emissions from the wide jet. Section 4 is devoted to a discussion. In this paper, we adopt cosmological parameters $H_0 = 71$ km s^{-1} Mpc^{-1}, $\Omega_M = 0.27$ and $\Omega_\Lambda = 0.23$ following Chand et al. (2020).

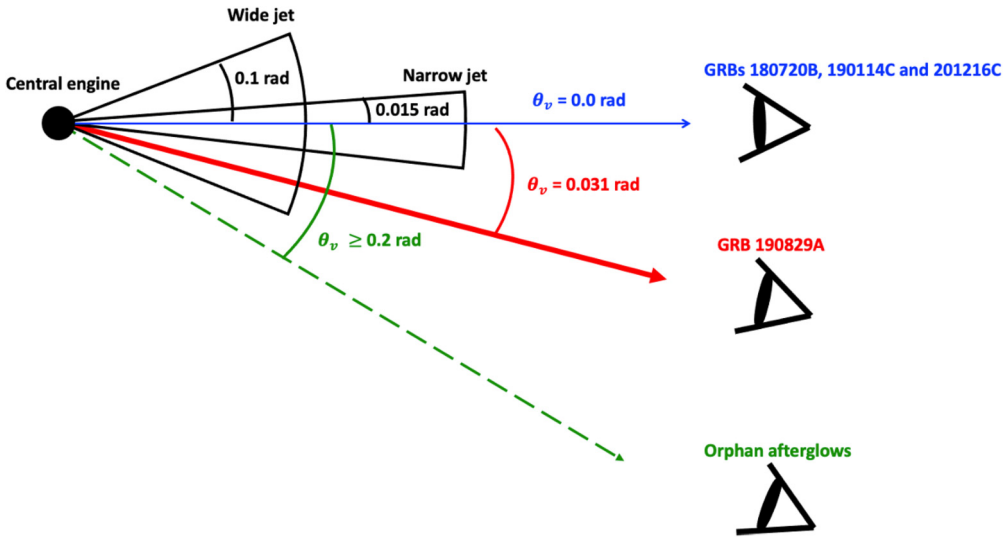

Fig. 1. Schematic view of our two-component jet model for very-high-energy GRBs. The afterglows of GRB 190829A are off-axis ($\theta_v = 0.031$ rad, thick red solid arrow) emissions. GRBs 180720B, 190114C and 201216C are observed in the case of on-axis viewing ($\theta_v = 0.0$ rad, thin blue solid arrow). Orphan afterglows are detected by viewed off-axis ($\theta_v \geq 0.2$ rad, thin green dashed arrow).

2. Numerical methods

We calculate the dynamics of a relativistic jet, which has an infinitely thin shell, following Huang et al. (2000) (see Sato et al., 2021, for details). The jet propagates into the ISM with a constant number density n_0, and it has an isotropic-equivalent kinetic energy $E_{\rm iso,K}$, initial bulk Lorentz factor Γ_0 and initial opening half-angle θ_0. A thin shell is formed as the jet expands. The synchrotron radiation is computed by using a power-law electron energy distribution with an index p and constant microphysics parameters ϵ_e, ϵ_B and f_e, which are the energy fractions of the internal energy going into power-law electrons and magnetic field, and the number fraction of accelerated electrons, respectively. In Sato et al. (2021), the number fraction of accelerated electrons f_e was fixed to be unity. In this paper, we consider the case of $f_e \neq 1.0$ to better explain the observed radio emissions.

In the calculation of the VHE gamma-ray radiation, the SSC emission is assumed (Sari and Esin, 2001). The SSC flux is affected by the Klein-Nishina effect (e.g. Blumenthal and Gould, 1970; Nakar et al., 2009; Murase et al., 2010, 2011; Wang et al., 2010; Zhang et al., 2021b; Jacovich et al., 2021). In Sato et al. (2021), the SSC radiation is estimated in the Thomson limit, while, in this paper, we take into account the Klein-Nishina effect using the numerical method given by Zhang et al. (2021b) (see Appendix of Zhang et al., 2021b, for details). We compare our numerical code with another in Zhang et al. (2021b). Our SSC and synchrotron cooling time is consistent with Zhang et al. (2021b) within $\sim 2\%$. Here we adopt Huang et al. (2000) in calculating the dynamics, while Zhang et al. (2021b) uses the dynamical evolution model by Nava et al. (2013), however, the behavior of our light curve is only slightly different from Zhang et al. (2021b). The extragalactic background light (EBL) absorption is considered in the calculation of the VHE gamma-ray flux. We adopt the model in Franceschini et al. (2008) and use 'EBL table'.[1]

Sato et al. (2021) proposed a two-component jet model, which consists of the narrow-fast ($\theta_0 = 0.015$ rad and $\Gamma_0 = 350$) and wide-slow ($\theta_0 = 0.1$ rad and $\Gamma_0 = 20$) jets. We assume that both jets are uniform, and on co-axis, and they are emitted from the central engine at the same time. The emissions are integrated along the equal arrival time surfaces (EATS) in calculation of the flux density F_ν (see Granot et al., 1999, for details).

3. Results of afterglow emission

In this section, we show our numerical results of afterglow emissions. In § 3.1, the observed light curves of GRB 190829A are compared with our results. In § 3.2, our multi-wavelength afterglow emissions for GRBs 180720B, 190114C and 201216C are exhibited, and we show that the VHE gamma-ray events are well explained by our two-component jet with similar parameters as those for GRB 190829A. In § 3.3, we discuss the detectability of off-axis orphan afterglows by changing the viewing angle in order to indicate the existence of our wide jet.

3.1. GRB 190829A

In this sub-section, we show our numerical results of afterglow emissions in the VHE gamma-ray (0.1 TeV), X-ray (5 keV), optical (V-band) and radio (1.3, 5.5, 15.5 and 99.8 GHz) bands, and together with the observed data of GRB 190829A. The VHE gamma-ray data are taken from H.E.S.S. Collaboration (2021). We convert the observed energy flux in 0.2–4.0 TeV to the flux density at 0.1 TeV assuming that the photon index is 2.2 at any time (H.E.S.S. Collaboration, 2021). The X-ray data are downloaded from the *Swift* team website[2] (Evans et al., 2007, 2009). The observed energy flux in 0.3–10 keV is converted to the flux density in 5 keV. We assume that the photon index is 2.2 at any time, and it is coincident with the observed data. The optical data are extracted from Chand et al. (2020). We adopt the V-band extinction $A_{\rm V} = 1.5$ mag (Chand et al., 2020). The radio flux at 5.5 and 99.8 GHz bands and at 1.3 and 15.5 GHz bands are measured by Dichiara et al. (2022) and Rhodes et al. (2020), respectively.

In this paper, we consider the Klein-Nishina effect in calculating the SSC process, and we do not fix f_e to be unity. The parameters determined by Sato et al. (2021) are somewhat modified. Early X-ray and optical afterglow emissions are well explained by the narrow jet with $\theta_v = 0.031$ rad, $\theta_0 = 0.015$ rad, $E_{\rm iso,K} = 4.0 \times 10^{53}$ erg, $\Gamma_0 = 350$, $n_0 = 0.01$ cm^{-3}, $p = 2.44$, $\epsilon_B = 6.0 \times 10^{-5}$, $\epsilon_e = 3.5 \times 10^{-2}$ and $f_e = 0.2$. A two-component jet

[1] https://pypi.org/project/ebltable/.

[2] https://www.swift.ac.uk/xrt_curves/00922968/.

model is considered in this work, in which another 'wide jet' is introduced. The parameters of the wide jet are $\theta_v = 0.031$ rad, $\theta_0 = 0.1$ rad, $E_{\rm iso,K} = 1.0 \times 10^{53}$ erg, $\Gamma_0 = 20$, $n_0 = 0.01$ cm^{-3}, $p = 2.2$, $\epsilon_B = 1.0 \times 10^{-5}$, $\epsilon_e = 0.29$ and $f_e = 0.35$. The superposition of each jet emission is compared with the observed light curve.

The numerical results of Sato et al. (2021) with $f_e = 1.0$ in 1.3 and 15.5 GHz bands exceeded the observed data within about a factor of three. We modify the value of f_e from 1.0 (Sato et al., 2021) to 0.2 and 0.35 for the narrow and wide jets, respectively. The value of the typical frequency ν_m in the case of $f_e \neq 1.0$ is larger than that in the case of $f_e = 1.0$. After $t \sim 10^5$ s, the typical and absorption frequencies, ν_m and ν_a, respectively, satisfy $\nu_a < 1.3$ GHz and 15.5 GHz $< \nu_m$. Then, the fluxes in 1.3 and 15.5 GHz bands depend on f_e ($F_\nu \propto {f_e}^{5/3}$). The radio fluxes are dim in the case of $f_e < 1.0$. As a result, our numerical light curves better match with the observed ones (orange and green lines in Fig. 2). Moreover, the late ($t \sim 10^{6-7}$ s) X-ray emission calculated in Sato et al. (2021) was about a factor of two smaller than the observed flux. The numerically calculated X-ray light curve is also improved by taking care of the Klein-Nishina effect (red lines in Fig. 2). When the Klein-Nishina effect is taken into account, the cooling frequency ν_c becomes larger because of less cooling compared with the Thomson limit. Since the X-ray band exceeds ν_c, the X-ray flux becomes brighter.

The VHE gamma-ray and X-ray fluxes are affected by the Klein-Nishina effect. The observed light curves in VHE gamma-ray and X-ray bands are well explained (magenta and red lines in Fig. 2). We consider the 99.8 and 5.5 GHz fluxes, which had not yet been reported in Sato et al. (2021). The narrow jet becomes trans-relativistic ($\Gamma < 10$) at $t \sim 10^5$ s, and the relation among the absorption frequency ν_a, the typical frequency ν_m and the cooling frequency ν_c satisfy $\nu_a < \nu_m < \nu_c$. The typical frequency ν_m depends on time t, and it crosses 99.8 GHz around 1.5×10^5 s. Then, the 99.8 GHz light curve has a peak. After that, ν_m is lower than 99.8 GHz band and the flux obeys the scaling $F_\nu \propto t^{-p} = t^{-2.44}$ (Gao et al., 2013). The observed data in 99.8 GHz decays slower than our numerical result. It is hard for the narrow jet to explain the observed data (brown dashed line in Fig. 2). The wide jet becomes trans-relativistic around $t \sim 10^5$ s and enters the Newtonian phase at $t \sim 2.0 \times 10^6$. From 10^5 to 10^7 s, the break frequencies ν_a, ν_m and ν_c satisfy the relation $\nu_a < \nu_m < \nu_c$. The value of ν_m crosses 99.8 GHz band around 2.5×10^5 s, at which the flux takes maximum and after that it follows as $F_\nu \propto t^{-3(5p-7)/10} = t^{-1.2}$ (Gao et al., 2013) (brown dotted line in Fig. 2). The sum of the narrow and wide jet emissions is coincident with the observed 99.8 GHz afterglow (brown solid line in Fig. 2). Subsequently, ν_m for the narrow and wide jet emissions crosses 5.5 GHz at 8.0×10^5 s and 5.5×10^6 s, respectively, and then their light curves have maxima, after which they decay in the same way as 99.8 GHz band (violet dashed and dotted lines in Fig. 2). The observed 5.5 GHz light curve is explained by the sum of both components (violet solid line in Fig. 2).

3.2. GRB 180720B, GRB 190114C and GRB 201216C

In § 3.1, the observational results of GRB 190829A are explained by our two-component jet model. We use our model described in § 3.1 to show that the VHE gamma-ray (0.1 TeV), high-energy (HE) gamma-ray (0.5 GeV), X-ray (5 keV and 500 keV), optical (r-band) and radio (9 and 10 GHz) afterglows of GRB 180720B, 190114C and 201216C are also well explained by similar parameters. In particular, we fix the opening angles and initial Lorentz factors of both jets as in the previous sub-section.

The X-ray (5 keV) data of the three events are obtained from the *Swift* team website. The VHE gamma-ray (0.1–0.44 TeV), HE gamma-ray (0.1–10 GeV) and optical (r-band) data of GRB 180720B are extracted from Abdalla et al. (2019). The observational data of GRB 190114C in the VHE gamma-ray (0.2–1 TeV), HE gamma-ray (0.1–1 GeV), hard X-ray (10–1000 keV), optical (r-band) and radio (9 GHz) bands are taken from MAGIC Collaboration (2019a). The optical (r-band) and radio (10 GHz) data of GRB 201216C are derived from Rhodes et al. (2022). We assume the r-band extinction $A_r = 0.8$ mag for GRBs 180720B and 190114C, and $A_r = 1.8$ mag for GRB 201216C. Redshifts are $z = 0.653$, 0.4245, and 1.1 for GRBs 180720B (Abdalla et al., 2019), 190114C (MAGIC Collaboration, 2019a) and 201216C (Blanch et al., 2020b), respectively. Adopted parameters, as well as those by previous works, are summarized in Tables 1, 2 and 3.

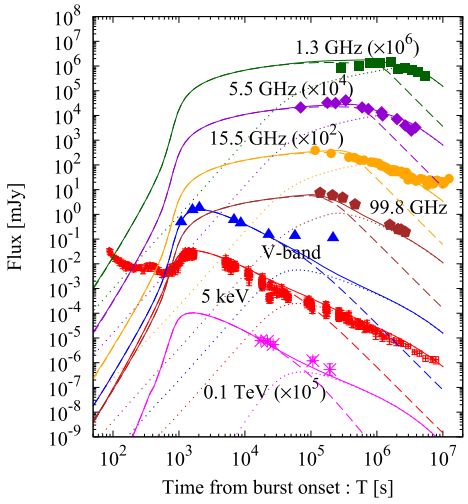

Fig. 2. Observed data of GRB 190829A (VHE gamma-ray (0.1 TeV: magenta points), X-ray (5 keV: red points), optical (V-band: blue triangles), radio bands (1.3 GHz: green squares, 5.5 GHz: violet diamonds, 15.5 GHz: orange filled-circles, 99.8 GHz: brown pentagons)), together with multi-wavelength afterglow modeling (VHE gamma-ray (0.1 TeV: magenta), X-ray (5 keV: red), optical (V-band: blue), radio bands (1.3 GHz: green, 5.5 GHz: violet, 5.5 GHz: orange, 99.8 GHz: brown)). Afterglow light curves calculated by our two-component jet model – solid lines are the sum of the narrow jet (dashed lines: $\theta_v = 0.031$ rad, $\theta_0 = 0.015$ rad, $E_{\rm iso,K} = 4.0 \times 10^{53}$ erg, $\Gamma_0 = 350$, $n_0 = 0.01$ cm^{-3}, $p = 2.44$, $\epsilon_B = 6.0 \times 10^{-5}$, $\epsilon_e = 3.5 \times 10^{-2}$, and $f_e = 0.2$) and wide jet (dotted lines: $\theta_v = 0.031$ rad, $\theta_0 = 0.1$ rad, $E_{\rm iso,K} = 1.0 \times 10^{53}$ erg, $\Gamma_0 = 20$, $n_0 = 0.01$ cm^{-3}, $p = 2.2$, $\epsilon_B = 1.0 \times 10^{-5}$, $\epsilon_e = 0.29$, and $f_e = 0.35$).

For GRB 180720B, we adopt the narrow jet with $n_0 = 10.0$ cm^{-3}, $p = 2.4$, $\epsilon_B = 5.0 \times 10^{-4}$, $\epsilon_e = 5.0 \times 10^{-3}$ and $f_e = 0.2$. The wide jet is introduced with the parameters, $p = 2.2$, $\epsilon_B = 9.0 \times 10^{-4}$, $\epsilon_e = 9.0 \times 10^{-2}$ and $f_e = 0.4$. These values of p, $E_{\rm iso,K}$ and ϵ_B of Wang et al. (2019) are almost close to ours, while our n_0 is larger than Wang et al. (2019).

For GRB 190114C, the parameters of $n_0 = 3.0$ cm^{-3}, $p = 2.8$, $\epsilon_B = 6.0 \times 10^{-5}$, $\epsilon_e = 9.0 \times 10^{-3}$ and $f_e = 0.1$ are adopted for the narrow jet. The wide jet with $p = 2.6$, $\epsilon_B = 9.0 \times 10^{-4}$, $\epsilon_e = 8.0 \times 10^{-2}$ and $f_e = 0.2$ are used. Parameters adopted by MAGIC Collaboration (2019a), Wang et al. (2019) and Asano et al. (2020) are roughly similar to our parameters, n_0, p, $E_{\rm iso,K}$, ϵ_B and ϵ_e. In MAGIC Collaboration (2019a) and Wang et al. (2019), the number fraction of accelerated electrons was adopted as $f_e = 1.0$, while in Asano et al. (2020) and this paper, it is calculated with $f_e \neq 1.0$. When the values of $E_{\rm iso,K}/f_e$, $f_e\epsilon_B$, $f_e\epsilon_e$ and n_0/f_e are same, the

Table 1
Parameters for modeling of GRB 180720B.

	n_0 [cm^{-3}]	p	$E_{\rm iso,K}$ [erg]	ϵ_B	ϵ_e	f_e
Present work (narrow jet)	10.0	2.4	4.0×10^{53}	5.0×10^{-4}	5.0×10^{-3}	0.2
Present work (wide jet)		2.2	1.0×10^{53}	9.0×10^{-4}	9.0×10^{-2}	0.4
Wang et al. (2019)	0.1	2.4	1.0×10^{54}	1.0×10^{-4}	0.1	1.0

behaviors of afterglow light curves are similar (Eichler and Waxman, 2005). The SSC flux with small ϵ_B is brighter than that with large ϵ_B, so that VHE gamma-ray events may have small ϵ_B (Miceli and Nava, 2022). In particular, we compare the value of $f_e\epsilon_B$ in the case of $f_e \neq 1.0$. For our narrow and wide jet parameters, we get $f_e\epsilon_B \sim 6.0 \times 10^{-6}$ and $\sim 1.8 \times 10^{-4}$, respectively. In Asano et al. (2020), $f_e\epsilon_B \sim 2.7 \times 10^{-4}$ was obtained. The value of $f_e\epsilon_B$ for our narrow jet is small like that of Asano et al. (2020), while that of our wide jet and Asano et al. (2020) is similar. Previous works (MAGIC Collaboration, 2019a; Wang et al., 2019; Asano et al., 2020) supposed a single component. In MAGIC Collaboration (2019a), the theoretically calculated radio emissions are about an order of magnitude brighter than the observed ones. Wang et al. (2019) and Asano et al. (2020) did not discuss the radio emission. In the present work, it is found that the two-component jet model well explains the observational radio flux.

For GRB 201216C, we use $n_0 = 1.0$ cm^{-3}, $p = 2.3$, $\epsilon_B = 6.0 \times 10^{-5}$, $\epsilon_e = 3.5 \times 10^{-2}$ and $f_e = 0.4$ in the narrow jet. The parameters of the wide jet are $p = 2.8$, $\epsilon_B = 5.0 \times 10^{-5}$, $\epsilon_e = 0.1$ and $f_e = 0.2$. Huang (2022) obtained parameters considering EATS effect, and the values of n_0, p, $E_{\rm iso,K}$ and ϵ_B are almost consistent with ours. In Rhodes et al. (2022), the jet-cocoon model was adopted. In particular, the narrow-core component ($\Gamma_0 > 100$) explained the observed afterglow in the X-ray and optical, while the wider low-energy component ($\Gamma_0 < 10$) was consistent with the radio emission. The value of $E_{\rm iso,K}$ of our wide jet is larger than that of the cocoon component of Rhodes et al. (2022). The stellar wind environment was considered in Rhodes et al. (2022), and then, the density in front of the shell is $\sim 10^{3-5}$ cm^{-3} at 10 days. Then, for both Rhodes et al. (2022) and our wide jet parameter, the absorption frequency ν_a is larger than 10 GHz, and the flux depends on $E_{\rm iso,K}$ and n_0 ($F_\nu \propto E_{\rm iso,K}^{5/6}\ {n_0}^{1/2}$). The flux with large $E_{\rm iso,K}$ and small n_0 is consistent with the flux in the case of small $E_{\rm iso,K}$ and large n_0, so that the observed radio flux of GRB 201216C is also explained by our wide jet with different values of $E_{\rm iso,K}$ and n_0 from Rhodes et al. (2022).

As seen in Fig. 3(a), the narrow jet explains the early time ($t \lesssim 2.0 \times 10^3$ s) observational results of GRB 180720B in the HE gamma-ray and X-ray bands, while the VHE gamma-ray, X-ray and optical emissions from the wide jet are consistent with the observed data at the late ($t \gtrsim 5.0 \times 10^3$ s) epoch. For GRB 190114C, the early ($t \lesssim 6.0 \times 10^3$ s) observed VHE gamma-ray, X-ray (5 keV) and optical fluxes are consistent with the narrow jet emissions, and at the late time ($t \gtrsim 6.0 \times 10^3$ s) the wide jet described the observed light curves in the X-ray (5 keV) and optical bands (see Fig. 3(b)). The early ($t \lesssim 3.0 \times 10^4$ s) and late ($t \gtrsim 10^5$ s) observational results in the radio band are well matched by the narrow and wide jets, respectively. Our narrow jet also fits with the observed data in the hard X-ray (500 keV) band ($t > 10$ s). As seen in Fig. 3(c), the early ($t \lesssim 2.0 \times 10^4$ s) X-ray and optical afterglows of GRB 201216C are explained by the narrow jet, while the late ($t \gtrsim 10^6$ s) radio data is consistent with the wide jet emission. Therefore, the observational results of the three VHE gamma-ray events are consistent with our two-component jet model. For all VHE gamma-ray events, the wide jet is necessary.

3.3. Orphan afterglows

In § 3.1 and 3.2, it is shown that our two-component jet model well explains the observational results of the previous VHE gamma-ray events (GRBs 180720B, 190114C, 190829A and 201216C). The existence of the wide jet is common. If VHE gamma-ray events are accountable by our two-component jet, orphan afterglow emissions may be observed in the case of large off-axis viewing angle. In this sub-section, we study the detectability of off-axis orphan afterglow emissions from our two-component jet in the VHE gamma-ray, X-ray, optical and radio bands by CTA/LST, eROSITA, Rubin LSST, ZTF, ALMA, ngVLA and SKA, respectively. Throughout this sub-section, the g-band extinction is assumed as a typical value $A_g = 2.8$ mag.

The viewing angle θ_v should be larger than 0.1 rad, which corresponds to the value of the initial jet opening half-angle of the wide jet. This is necessary because the prompt emissions from the narrow and wide jets are not detected. Since the narrow jet has a small $\theta_0 = 0.015$ rad, the afterglow emissions from the narrow jet are dimmer than those from the wide jet. In this sub-section, the afterglow fluxes from the wide jet are considered.

When we change the viewing angle, $E_{{\rm iso},\gamma}(\theta_v)$ and $E_p(\theta_v)$ are estimated using the method given by Donaghy (2006), Graziani et al. (2006) and Ioka and Nakamura (2001) (see also Yamazaki et al., 2002, 2003a,b, 2004; Sato et al., 2021). Here we assume that the narrow and wide jets have the values of $E_{{\rm iso},\gamma}(\theta_v = 0.0$ rad) and $E_p(\theta_v = 0.0$ rad) based on our model for Episode 1 and 2 of GRB 190829A (Sato et al., 2021), that is $E_{{\rm iso},\gamma}(\theta_v = 0.0$ rad$) = 2.7 \times 10^{53}$ erg and $E_p(\theta_v = 0.0$ rad$) = 3.7$ MeV for the narrow jet, and $E_{{\rm iso},\gamma} = 1.9 \times 10^{50}$ erg and $E_p = 10.9$ keV for the wide jet. Then, we obtain off-axis ($\theta_v = 0.2$ rad) quantities are obtained as $E_{{\rm iso},\gamma}(\theta_v = 0.2$ rad$) = 1.3 \times 10^{48}$ erg and $E_p(\theta_v = 0.2$ rad$) = 1.5$ keV for the narrow jet, and $E_{{\rm iso},\gamma}(\theta_v = 0.2$ rad$) = 9.2 \times 10^{47}$ erg and $E_p(\theta_v = 0.2$ rad$) = 1.9$ keV for the wide jet. In the case of $\theta_v \geq 0.2$ rad, such low-energy prompt emission may be difficult to be detected unless the distance to the source is very nearby. In this sub-section, we use the wide jet parameters ($\theta_0 = 0.1$ rad, $E_{\rm iso,K} = 1.0 \times 10^{53}$ erg, $\Gamma_0 = 20$, $p = 2.2$, $\epsilon_B = 1.0 \times 10^{-5}$, $\epsilon_e = 0.29$, and $f_e = 0.35$), and change the viewing angle $\theta_v = 0.0$, 0.2 and 0.3 rad, the ISM density $n_0 = 0.01$ and 1.0 cm^{-3} and the redshift $z = 0.05$ and 0.5.

We consider the case of the observation with four CTA/LSTs (CTA/4 LSTs). Although CTA/4 LSTs are most sensitive around 2 TeV,[3] such high-energy photons are heavily absorbed by EBL. Here we draw the VHE gamma-ray light curves at $h\nu = 0.3$ TeV, since it is less affected by the EBL attenuation and it can be still observed with good sensitivity of CTA/4 LSTs. Fig. 4 shows the results. In the case of $z = 0.05$ (Fig. 4(a)), one can find that CTA/4 LSTs have the capability to detect off-axis ($\theta_v = 0.2$–0.3 rad) orphan afterglows if the ambient density is $n_0 = 1.0$ cm^{-3} (thick red dashed and dotted lines). Furthermore, the events from rarefied medium, $n_0 = 0.01$ cm^{-3}, viewed off-axis ($\theta_v = 0.2$ rad) can be also observed by CTA/4 LSTs (thin blue dashed line in Fig. 4(a)). For the source redshift $z = 0.5$, CTA/4 LSTs will detect the VHE gamma-rays from events with $n_0 = 1.0$ cm^{-3} and $\theta_v = 0.2$ rad (thick red dashed line in Fig. 4(b)). Due to the EBL attenuation, the 0.3 TeV flux from the source at $z = 0.5$ becomes about an order of magnitude smaller than the unabsorbed one. Orphan af-

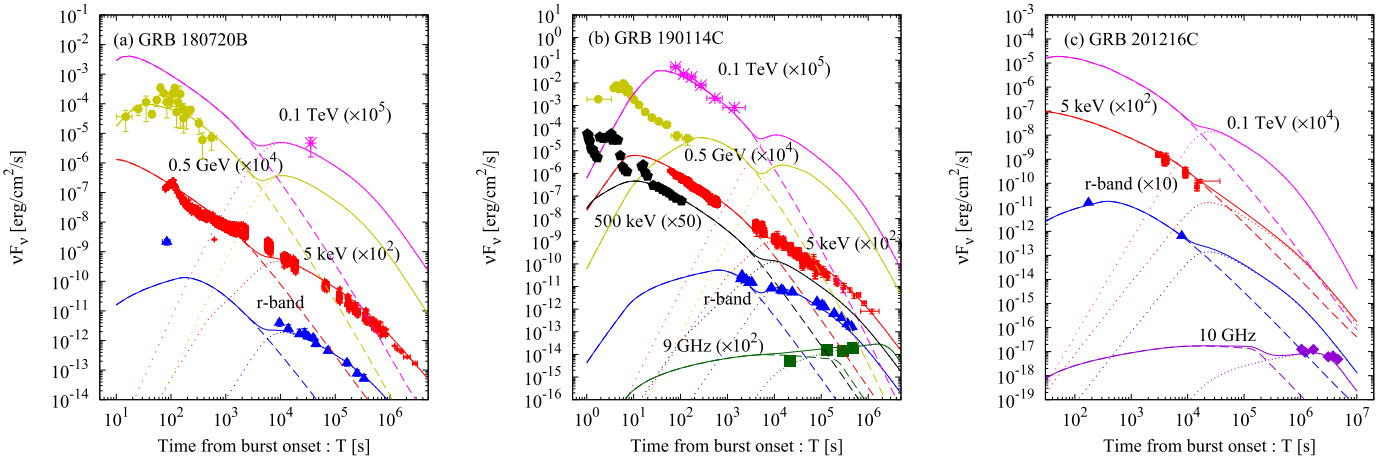

Fig. 3. Observed data (VHE gamma-ray (0.1 TeV: magenta points), HE gamma-ray (0.5 GeV: yellow filled-circles), X-ray (5 keV: red points and 500 keV: black pentagons), optical (r-band: blue triangles) and radio bands (9 GHz: green squares and 10 GHz: violet diamonds)) of GRB 180720B (panel (a)), 190114C (panel (b)) and 201216C (panel (c)), together with afterglow light curves calculated by our two-component jet model – solid lines are the sum of the narrow (dashed lines) and wide (dotted lines) jets in the VHE gamma-ray (0.1 TeV: magenta), HE gamma-ray (0.5 GeV yellow), X-ray (5 keV: red and 500 keV: black), optical (r-band: blue) and radio bands (1.3 GHz: green and 10 GHz: purple). The panel (a) (GRB 180720B) shows the result of our narrow ($\theta_v = 0.0$ rad, $\theta_0 = 0.015$ rad, $E_{\rm iso,K} = 4.0 \times 10^{53}$ erg, $\Gamma_0 = 350$, $n_0 = 10$ cm^{-3}, $p = 2.4$, $\epsilon_B = 5.0 \times 10^{-4}$, $\epsilon_e = 5.0 \times 10^{-3}$, and $f_e = 0.2$) and wide ($\theta_v = 0.0$ rad, $\theta_0 = 0.1$ rad, $E_{\rm iso,K} = 1.0 \times 10^{53}$ erg, $\Gamma_0 = 20$, $n_0 = 10$ cm^{-3}, $p = 2.2$, $\epsilon_B = 9.0 \times 10^{-4}$, $\epsilon_e = 0.09$, and $f_e = 0.4$) jets. In panel (b) (GRB 190114C), we show our result of the narrow ($\theta_v = 0.0$ rad, $\theta_0 = 0.015$ rad, $E_{\rm iso,K} = 4.0 \times 10^{53}$ erg, $\Gamma_0 = 350$, $n_0 = 3$ cm^{-3}, $p = 2.8$, $\epsilon_B = 6.0 \times 10^{-5}$, $\epsilon_e = 9.0 \times 10^{-3}$, and $f_e = 0.1$) and wide ($\theta_v = 0.0$ rad, $\theta_0 = 0.1$ rad, $E_{\rm iso,K} = 1.0 \times 10^{53}$ erg, $\Gamma_0 = 20$, $n_0 = 3$ cm^{-3}, $p = 2.6$, $\epsilon_B = 9.0 \times 10^{-4}$, $\epsilon_e = 8.0 \times 10^{-2}$, and $f_e = 0.2$) jets. In panel (c) (GRB 201216C), the sum of the narrow ($\theta_v = 0.0$ rad, $\theta_0 = 0.015$ rad, $E_{\rm iso,K} = 4.0 \times 10^{53}$ erg, $\Gamma_0 = 350$, $n_0 = 1$ cm^{-3}, $p = 2.3$, $\epsilon_B = 6.0 \times 10^{-5}$, $\epsilon_e = 3.5 \times 10^{-2}$, and $f_e = 0.4$) and wide ($\theta_v = 0.0$ rad, $\theta_0 = 0.1$ rad, $E_{\rm iso,K} = 1.0 \times 10^{53}$ erg, $\Gamma_0 = 20$, $n_0 = 1$ cm^{-3}, $p = 2.8$, $\epsilon_B = 5.0 \times 10^{-5}$, $\epsilon_e = 0.1$, and $f_e = 0.2$) jets are shown.

Table 2
Parameters for modeling of GRB 190114C.

	n_0 [cm^{-3}]	p	$E_{\rm iso,K}$ [erg]	ϵ_B	ϵ_e	f_e
Present work (narrow jet)	3.0	2.8	4.0×10^{53}	6.0×10^{-5}	9.0×10^{-3}	0.1
Present work (wide jet)		2.6	1.0×10^{53}	9.0×10^{-4}	8.0×10^{-2}	0.2
MAGIC Collaboration (2019a)	0.5–5	2.4–2.6	$\gtrsim 3.0 \times 10^{53}$	$(0.05–1.0) \times 10^{-3}$	0.05–0.15	1.0
Wang et al. (2019)	0.3	2.5	6.0×10^{53}	4.0×10^{-5}	7.0×10^{-2}	1.0
Asano et al. (2020)	1.0	2.3	1.0×10^{54}	9.0×10^{-4}	6.0×10^{-2}	0.3

Table 3
Parameters for modeling of GRB 201216C.

	n_0 [cm^{-3}]	p	$E_{\rm iso,K}$ [erg]	ϵ_B	ϵ_e	f_e
Present work (narrow jet)	1.0	2.3	4.0×10^{53}	6.0×10^{-5}	3.5×10^{-2}	0.4
Present work (wide jet)		2.8	1.0×10^{53}	5.0×10^{-5}	0.1	0.2
Huang (2022) (EATS)	0.5	2.1	6.0×10^{53}	8.0×10^{-5}	0.6	1.0
Rhodes et al. (2022) (narrow-core component)	(wind)	2.0–2.4	$(0.6 - 10) \times 10^{52}$	$(0.05–4.0) \times 10^{-3}$	0.04–0.1	1.0
Rhodes et al. (2022) (cocoon component)	(wind)	2.0	$(0.02–50) \times 10^{48}$	1.0×10^{-2}	0.1	1.0

terglows with higher redshifts ($z > 0.5$) are hard to be detected with CTA/4 LSTs.

We roughly estimate the detection rate of orphan afterglows arising within $z = 0.5$ by CTA/4 LSTs. CTA/LST has a field of view of 2.5°[3] with a duty cycle of 10% (Cherenkov Telescope Array Consortium et al., 2019). We set the comoving rate density $R_{\rm GRB} \sim$ 300 Gpc^{-3} yr^{-1} and the solid angle subtended by the direction to which the source is observed $f_\Omega = 5.0 \times 10^{-3}$ sr. Then, the expected detection rate by CTA within $z = 0.5$ (luminosity distance $d_L \sim 2.8$ Gpc) is simply given by

$$\dot{N}_{\rm GRB} \sim \frac{4\pi}{3} R_{\rm GRB}\, d_L^3\, f_\Omega\, \frac{(\theta_{\rm FOV})^2}{2}\, DC$$
$$\sim 0.15\ {\rm yr}^{-1} \left(\frac{R_{\rm GRB}}{300\ {\rm Gpc^{-3}\ yr^{-1}}}\right)\left(\frac{d_L}{2.8\ {\rm Gpc}}\right)^3$$
$$\times \left(\frac{f_\Omega}{5.0 \times 10^{-3}\ {\rm sr}}\right)\left(\frac{\theta_{\rm FOV}}{2.5^\circ}\right)^2\left(\frac{DC}{10\%}\right), \quad (1)$$

where $\theta_{\rm FOV}$ is a field of view and DC is the duty cycle.

We also calculate the X-ray, optical and radio (16 and 343 GHz) fluxes with the same parameters as shown in Fig. 4. It is found from Figs. 5, 6, 7 and 8 that they are bright enough to be detected by eROSITA, Rubin LSST, ZTF, ALMA, ngVLA and SKA when $z = 0.5$. Therefore, when CTA/4 LSTs detect orphan afterglows, multi-wavelength observations are capable with eROSITA, Rubin LSST, ZTF, ALMA, ngVLA and SKA.

4. Discussion

We found that the observed VHE gamma-ray emission of GRB 190829A could be explained only by the SSC radiation. If the isotropic-equivalent gamma-ray energy $E_{{\rm iso},\gamma}(\theta_v)$ and peak energy $E_p(\theta_v)$ viewed on-axis ($\theta_v = 0.0$ rad) are small, then, the total intrinsic energy is too small to explain the observed VHE

[3] https://zenodo.org/record/5499840#.Y0TaWi0RodV.

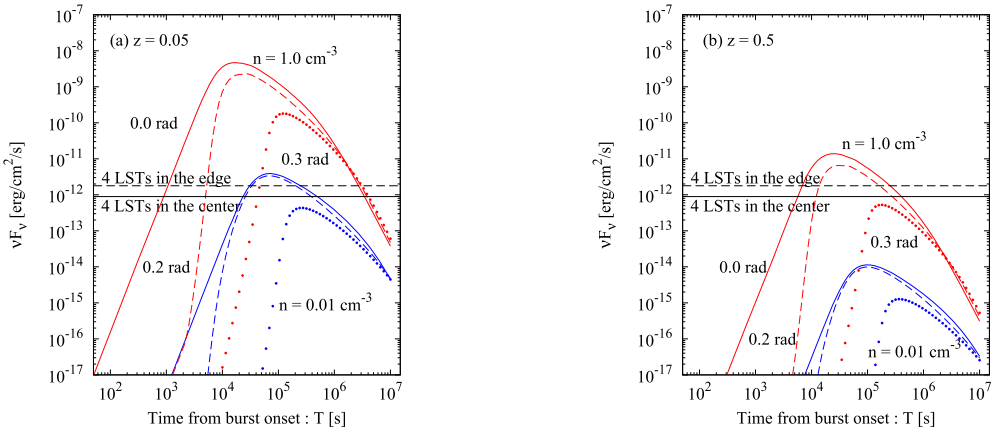

Fig. 4. VHE gamma-ray light curves at $h\nu$ =0.3 TeV from the 'wide jet' ($\theta_0 = 0.1$ rad, $E_{\rm iso,K} = 1.0 \times 10^{53}$ erg, $\Gamma_0 = 20$, $p = 2.2$, $\epsilon_B = 1.0 \times 10^{-5}$, $\epsilon_e = 0.29$, and $f_e = 0.35$) at $z = 0.05$ (panel (a)) and 0.5 (panel (b)). The thick red and thin blue lines show the results for the ISM density $n_0 = 1.0$ and 0.01 cm^{-3}, respectively. The solid, dashed and dotted lines are for cases of viewing angle $\theta_v = 0.0$, 0.2 and 0.3 rad, respectively. Sensitivities of CTA/4 LSTs at the center (black solid line) and CTA/4 LSTs at the near edge (black dashed line) of the observation field of view are shown assuming an exposure time of three hours.[3]

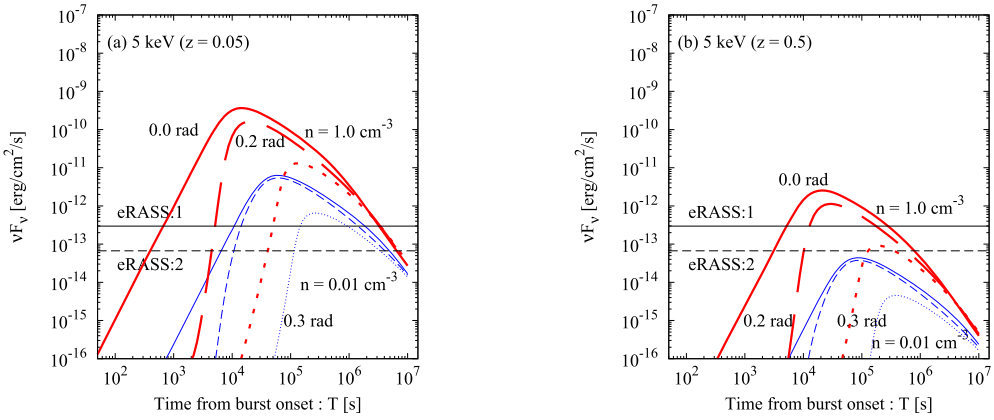

Fig. 5. X-ray light curves at $h\nu$ =5 keV from the 'wide jet' ($\theta_0 = 0.1$ rad, $E_{\rm iso,K} = 1.0 \times 10^{53}$ erg, $\Gamma_0 = 20$, $p = 2.2$, $\epsilon_B = 1.0 \times 10^{-5}$, $\epsilon_e = 0.29$, and $f_e = 0.35$) at $z = 0.05$ (panel (a)) and 0.5 (panel (b)). The thick red and thin blue lines show the results for the ISM density $n_0 = 1.0$ and 0.01 cm^{-3}, respectively. The solid, dashed and dotted lines are for cases of viewing angle $\theta_v = 0.0$, 0.2 and 0.3 rad, respectively. Sensitivities of eRASS: 1 (black solid line) and eRASS: 2 (black dashed line) are shown assuming an exposure time of 500 s (Merloni, 2012).

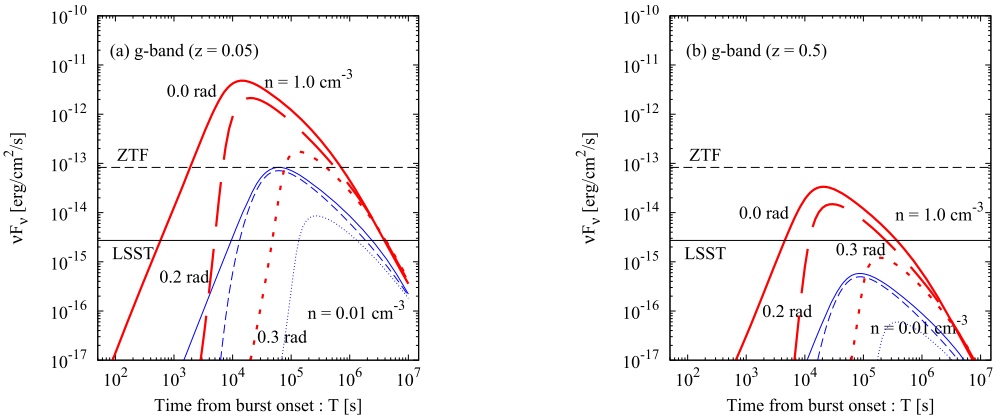

Fig. 6. Optical light curves at g-band from the 'wide jet' ($\theta_0 = 0.1$ rad, $E_{\rm iso,K} = 1.0 \times 10^{53}$ erg, $\Gamma_0 = 20$, $p = 2.2$, $\epsilon_B = 1.0 \times 10^{-5}$, $\epsilon_e = 0.29$, and $f_e = 0.35$) at $z = 0.05$ (panel (a)) and 0.5 (panel (b)). The thick red and thin blue lines show the results for the ISM density $n_0 = 1.0$ and 0.01 cm^{-3}, respectively. The solid, dashed and dotted lines are for cases of viewing angle $\theta_v = 0.0$, 0.2 and 0.3 rad, respectively. Sensitivities of Rubin LSST (black solid line) (Ivezić et al., 2019) and ZTF (black dashed line) (Bellm et al., 2019) are shown assuming an exposure time of 140 s.

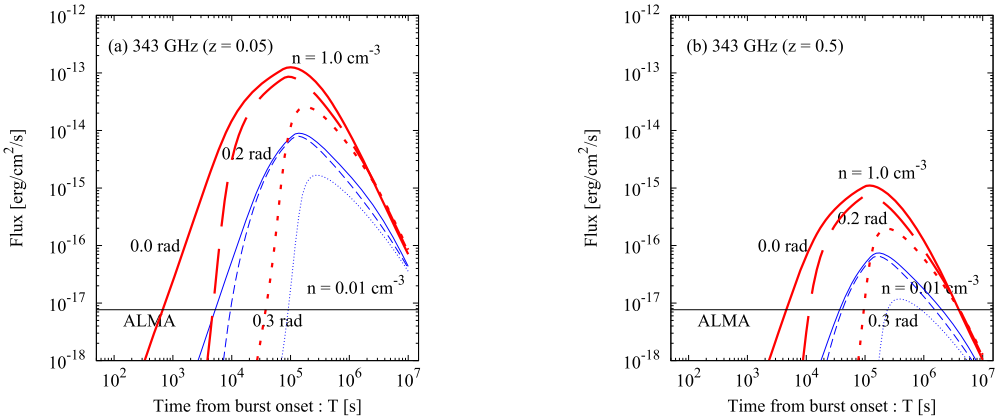

Fig. 7. Radio light curves at 343 GHz from the 'wide jet' ($\theta_0 = 0.1$ rad, $E_{\rm iso,K} = 1.0 \times 10^{53}$ erg, $\Gamma_0 = 20$, $p = 2.2$, $\epsilon_B = 1.0 \times 10^{-5}$, $\epsilon_e = 0.29$, and $f_e = 0.35$) at $z = 0.05$ (panel (a)) and 0.5 (panel (b)). The thick red and thin blue lines show the results for the ISM density $n_0 = 1.0$ and 0.01 cm^{-3}, respectively. The solid, dashed and dotted lines are for cases of viewing angle $\theta_v = 0.0$, 0.2 and 0.3 rad, respectively. Sensitivity of ALMA (black solid line) is shown assuming an exposure time of 100 hours.[4]

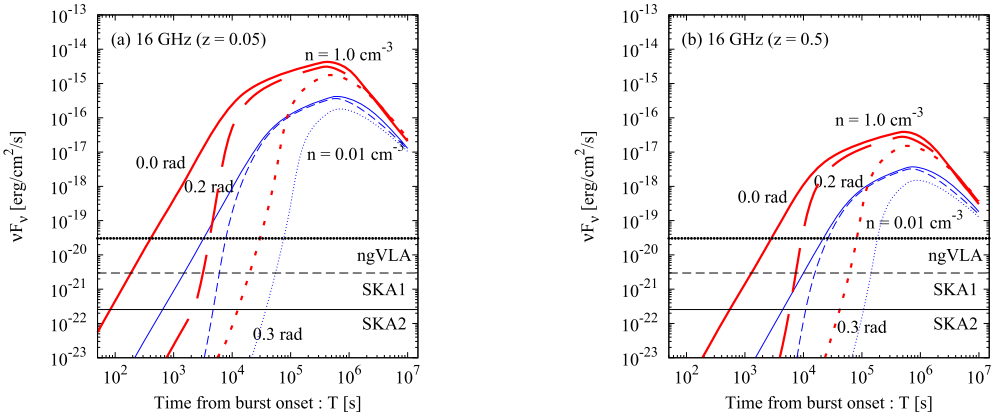

Fig. 8. Radio light curves at 16 GHz from the 'wide jet' ($\theta_0 = 0.1$ rad, $E_{\rm iso,K} = 1.0 \times 10^{53}$ erg, $\Gamma_0 = 20$, $p = 2.2$, $\epsilon_B = 1.0 \times 10^{-5}$, $\epsilon_e = 0.29$, and $f_e = 0.35$) at $z = 0.05$ (panel (a)) and 0.5 (panel (b)). The thick red and thin blue lines show the results for the ISM density $n_0 = 1.0$ and 0.01 cm^{-3}, respectively. The solid, dashed and dotted lines are for cases of viewing angle $\theta_v = 0.0$, 0.2 and 0.3 rad, respectively. Sensitivities of ngVLA (black dotted line) (Selina et al., 2018), SKA1 (black dashed line) and SKA2 (black solid line) (Chen et al., 2021) are shown assuming an exposure time of 100 hours.

gamma-ray flux of GRB 190829A by the SSC radiation (Zhang et al., 2021b). However, we have supposed that the jetted prompt emission of GRB 190829A would have been $E_{\rm iso,\gamma}(\theta_v = 0.0$ rad) and $E_p(\theta_v = 0.0$ rad) of typical long GRBs if our narrow jet were viewed on-axis. Since the total intrinsic energy had large, the VHE gamma-ray light curve was explained only by the SSC emission (magenta solid line in Fig. 2).

As seen in Fig. 2, our numerical radio (99.8 GHz) and VHE gamma-ray fluxes of GRB 190829A were sometimes dimmer than the observational result. However, they are only within a factor of two, and this difference may come from the limitation of the simple afterglow model. For example, if microphysics parameters ϵ_e, ϵ_B and f_e have time-dependent, this problem may be solved. A small density fluctuation may reconcile them. Our theoretical radio flux at 1.3 GHz overshot the observed one between 2.0×10^5 s $< t < 6.0 \times 10^5$ s. The excess was also within a factor of two and it may solve in the same manner. In Sato et al. (2021), we calculated the SSC cooling in the Thomson limit and fixed as $f_e = 1.0$. However, in this paper, the Klein-Nishina effect and the case of $f_e \neq 1.0$ were considered. The late ($t \sim 10^{6-7}$ s) X-ray and radio (1.3 GHz and 15.5 GHz) emissions of GRB 190829A have been improved (red, orange and green lines in Fig. 2).

After 5.0×10^6 s, the observed flux in 15.5 GHz of GRB 190829A was brighter than our result (see Fig. 2), and it may be a radio supernova. Type-Ic Supernova SN 2019oyw was associated with GRB 190829A (Hu et al., 2021). The peak luminosity of a typical type-Ic supernova is about 10^{28-29} erg s^{-1} Hz^{-1} at $t \sim 10^7$ s in radio band (Bietenholz et al., 2021) At 5.0×10^6 s, the luminosity of GRB 190829A in 15.5 GHz band is about 10^{29} erg s^{-1}, and it is consistent with the typical peak luminosity of the radio supernovae.

VLBI observations of GRB 190829A gave a constraint, $E_{\rm iso}/n_0 < 10^{56}$ erg cm^3 (Salafia et al., 2022). For our narrow and wide jet parameters, we get $E_{\rm iso}/n_0 = 4.0 \times 10^{55}$ erg cm^3 and 1.0×10^{55} erg cm^3, respectively, and they are consistent with the observational upper limit. Furthermore, source size upper limits (FWHM) in radio bands were obtained (Salafia et al., 2022). Here, we also simply estimate the apparent jet size as the following. The bulk Lorentz factor of the jet is initially so high that the jet size is calculated by $2R/\Gamma$. As the jet decelerates, the beaming effect becomes weak. The jet size is estimated as $2R\theta_j$, where θ_j is the jet opening half-angle. The jet full angular size is calculated as $2\ \min\{R/\Gamma,\ R\theta_j\}/d_A$, where d_A is the angular diameter distance to the source. The value of $2\ \min\{R/\Gamma,\ R\theta_j\}/d_A$, multiplied by 0.65, is roughly equal to the FWHM of the observed radio angular size for the uniform jet (Salafia et al., 2022). It is found that our result and observed data are consistent within 2σ range.

The upper limit on the linear polarization in the optical band of GRB 190829A was detected (Dichiara et al., 2022). In Dichiara

[4] https://asa.alma.cl/SensitivityCalculator/.

et al. (2022), they supposed that the value of the linear polarization in the off-axis viewing case was larger than the observed one. They adopted the model of Rossi et al. (2004), which assumed that the magnetic field generated by the Weibel instability is extremely anisotropic and turbulent. However, the magnetic field structure in the shock front is unclear. If the direction of the distribution of the magnetic field downstream of the shock is less anisotropic, the polarization of their model may be lower by a factor of 3-4 (Shimoda and Toma, 2021; Kuwata et al., 2022). The downstream magnetic field may not be formed by the Weibel instability. Then, the value of the polarization is much uncertain.

For GRB 190829A, the Fermi-LAT obtained upper limits in the HE range (Fraija et al., 2021). In our calculation, the numerical synchrotron radiation is brighter than the SSC emission at 1 GeV, and the numerical SSC flux dominates over the synchrotron component at 10 GeV in both the narrow and wide jets. Our numerical emissions both 1 and 10 GeV bands are dimmer than the sensitivity of Fermi-LAT.

Our two-component jet model in the cases of the on-axis viewing ($\theta_v = 0.0$ rad) but with different values of n_0, p, ϵ_e, ϵ_B and f_e well explained the observed light curves of GRBs 180720B, 190114C and 201216C (Figs. 3(a), (b) and (c)). For GRB 180720B, the first optical data point overshot our numerical result as well as Wang et al. (2019). It may be the contribution from the reverse-shock emission (Fraija et al., 2019b). After about $t \sim 80$ s, the HE gamma-ray flux of GRB 180720B decays steeply (Ronchi, 2020). The narrow jet well explained the observed HE gamma-ray data.

In GRB 190114C, the observed HE gamma-ray flux was brighter than our numerically calculated one. It is claimed that the prompt and reverse-shock emissions may contribute to the HE gamma-ray flux (Wang et al., 2019; Asano et al., 2020). The early ($t \sim 10^2 - 10^3$ s) bright optical flux of GRB 190114C was observed (Jordana-Mitjans et al., 2020; Shrestha, 2022). It is difficult for the forward shock emission from our two-component jet model to explain the early optical observation. Jordana-Mitjans et al. (2020) and Shrestha (2022) supposed that the early optical radiation may be the reverse-shock emission. In Wang et al. (2019) and Asano et al. (2020), the early ($t \lesssim 10^2$ s) observed X-ray (5 keV) afterglow exceeds their numerical results, while our X-ray (5 keV) emission from our narrow jet is consistent with observed data (red solid line in Fig. 3(b)). The late ($t \gtrsim 6.0 \times 10^3$ s) observed optical flux is brighter than the numerical result in Wang et al. (2019). Our wide jet is better consistent with the observed optical light curve (blue solid line in Fig. 3(b)) than previous theoretical works. Before 20 s, the numerically calculated flux at 500 keV is dimmer than the observed data. It may be the contribution of the prompt emission (MAGIC Collaboration, 2019a).

For GRB 201216C, the observed VHE gamma-ray flux has not been published. At 57 s when MAGIC detected the VHE gamma-ray photons, our numerical calculation gave the energy flux, $\nu F_\nu \sim 2.0 \times 10^{-9}$ erg cm^{-2} s^{-1}, at 0.1 TeV (magenta solid line in Fig. 3(c)). If our numerical VHE gamma-ray flux of GRB 201216C was consistent with the observed one, we confirm the validity of our two-component jet model. In this paper, the observed radio data of GRB 201216C was explained by a two-component jet model as well as Rhodes et al. (2022).

As seen in the yellow solid lines of Figs. 3(a) and (b), the HE gamma-ray light curves have the plateaus. The HE gamma-ray light curves with the plateau phase have been reported Ajello et al. (2019). According to our model, the two-component jet model is needed to explain complex multi-wavelength afterglow light curves of VHE gamma-ray GRBs. Furthermore, the values of $\epsilon_B \sim 10^{-5} - 10^{-4}$ and $E_{\rm iso,\ K} \sim 10^{53}$ erg are required for VHE gamma-ray emissions. The VHE gamma-ray events may have unique features.

We have supposed the two-component jet, which had the narrow-fast ($\theta_0 = 0.015$ rad and $\Gamma_0 = 350$) and wide-slow ($\theta_0 = 0.1$ rad and $\Gamma_0 = 20$) jets. The two-component jet model has two different photon fields, so that inprinciple the external inverse-Compton (EIC) emission might be non-negligible. If the two radiation regions have a large velocity difference, then, the EIC mechanism may have an important role (Ghisellini et al., 2005). At the time when GRB 190829A was detected by H.E.S.S., however, there was only a small difference of the bulk Lorentz factor between our two jets (see Fig. 3 in Sato et al., 2021). The VHE gamma-ray fluxes from our two-component jet are less influenced by the EIC component, so that the observed data of GRB 190829A could be explained only by the SSC emission. In our modeling, GRBs 180720B, 190114C and 201216C had the same θ_0, Γ_0 and $E_{\rm iso,\ K}$ as GRB 190829A, and n_0 of the three GRBs had similar values. Hence, the behaviors of the four-velocity $\Gamma\beta$ and radius R of the jets in these events are similar to those of GRB 190829A. The detection time of VHE gamma-ray photons of GRB 180720B ($t \sim 3.6 \times 10^4$ s) was later than that of GRB 190829A ($t \sim 2.0 \times 10^4$ s), so that the EIC component less affects the VHE gamma-ray flux of GRB 180720B as well as GRB 190829A. For GRB 190114C, from 57 s to 1591 s after the burst onset, the VHE gamma-ray emission was detected by MAGIC. In this paper, we considered that GRB 190114C was viewed on-axis. The bulk Lorentz factor of the narrow jet had still large from 57 s to 1591 s, so that the wide-jet synchrotron emission from behind is dim for the narrow jet due to the relativistic beaming effect. At the narrow jet, the energy density synchrotron photon density from the wide jet is much smaller than one of the narrow jet by itself. The EIC mechanism less affects the observational flux of GRB 190114C.

We confirmed that our two-component jet model was consistent with the observational results of GRBs 180720B, 190114C, 190829A and 201216C in § 3.1 and 3.2. The electron spectral index p of the narrow and wide jets might be different from each other, and then we may observe the change of the spectral index from one to another. It may be an indication of the existence of the two components. Another possibility is that we may observe the dip and/or bumps in light curves, which are difficult to be explained by the single component jet (Beniamini et al., 2020; Duque et al., 2022). Furthermore, late radio observations may be important to discriminate the two-component jet. The narrow jet emissions decay rapidly, and they are followed by late-time wide jet emissions.

As shown in Tables 1, 2 and 3, the narrow and wide jets have different microphysics parameters, ϵ_e, ϵ_B and f_e. They might depend on the properties of circumburst matter like the number density. However, at present, it is still unknown how their values are determined, and therefore, the dependence on the ambient medium is not clarified. There are several possibilities for making an anisotropic medium into which the two jets penetrate, resulting in their different microphysics parameters. If a progenitor star is rotating, a unique environment might be built along the rotational axis. Then, the magnetic fields and density could depend on the angle from the rotational axis. In addition, differences in the deceleration of the narrow and wide jets may affect microphysics parameters in the forward-shocked region because the non-linear evolution of the Rayleigh-Taylor instability affects the forward-shocked region. Inherent ejecta properties like magnetization parameters could be transferred into the emitting thin shell by mixing the ejecta and circumburst material. If the ejecta of the narrow and wide jets is different, the value of microphysics parameters of the narrow and wide jets could have different values.

In § 3.3, we calculated the event rate of the orphan afterglow emission by CTA/4 LSTs during the observations of other targets. Orphan afterglows are more likely to be detected at the edge of the field of view of CTA/4 LSTs. The sensitivity in the edge of the field of view of CTA/4 LSTs is about two times lower than that of

the center. Since the VHE gamma-ray flux exceeded the sensitivity in the edge of CTA/4 LSTs (thick red and thin blue lines Figs. 4(a) and (b)), the event rate may not be largely affected.

The light curves viewed on-axis ($\theta_v = 0.0$ rad) and off-axis ($\theta_v = 0.2$ and 0.3 rad) in the VHE gamma-ray, X-ray and optical bands have achromatic peaks (see solid, dashed and dotted lines in Figs. 4, 5 and 6). In the on-axis viewing case, the light curves have achromatic peaks when the transitions from the free-expansion to the Blandford-McKee phase (Sari, 1997). The observer time of the flux maximum is analytically given by Sari (1997)

$$t_{\rm peak,on} \sim (1+z)\left(\frac{3E_{\rm iso,K}}{32\pi n_0 m_p c^5 \Gamma_0^8}\right)^{1/3} \sim 1.5\times10^4 \left(\frac{1+z}{1.05}\right)\left(\frac{E_{\rm iso,K}}{10^{53}\ {\rm erg}}\right)^{1/3}\left(\frac{n_0}{1.0\ {\rm cm^{-3}}}\right)^{-1/3} \times\left(\frac{\Gamma_0}{20}\right)^{-8/3}\ {\rm s}\ . \quad (2)$$

The off-axis afterglows show the rising part because of the relativistic beaming effect. The observer time of the peak in the light curve for $\theta_v = 0.2$ rad is estimated by

$$t_{\rm peak,off} \sim (1+z)\left(\frac{3E_{\rm iso,K}}{32\pi n_0 m_p c^5}\right)^{1/3}\left(\frac{\theta_v-\theta_0}{2}\right)^{8/3} \sim 3.0\times10^4 \left(\frac{1+z}{1.05}\right)\left(\frac{E_{\rm iso,K}}{10^{53}\ {\rm erg}}\right)^{1/3}\left(\frac{n_0}{1.0\ {\rm cm^{-3}}}\right)^{-1/3} \times\left(\frac{\theta_v-\theta_0}{0.1\ {\rm rad}}\right)^{8/3}\ {\rm s}\ . \quad (3)$$

In the case of $\theta_v = 0.3$ rad, we obtain $t_{\rm peak,off} \sim 1.9\times10^5$ s. The emissions viewed with $\theta_v = 0.0$ and 0.2 rad have maximum almost at the same time, while the observer time at the peak in the case of $\theta_v = 0.3$ rad is later than the on-axis viewing ($\theta_v = 0.0$ rad) case. Other combinations of n_0 and z behave in the same manner. In the radio bands (16 and 343 GHz), each light curve has a peak when the typical frequency ν_m crosses 16 and 343 GHz bands, respectively. In particular, for $z = 0.05$ and $n_0 = 1.0$ cm^{-3}, ν_m intersects 16 GHz at $t \sim 5.0\times10^5$ s, and then, our numerical result in 16 GHz takes maximum (thick red lines in Figs. 7(a) and 8(a)).

We considered the jets which had the same wide jet parameters (p, $E_{\rm iso}$, ϵ_e, ϵ_B and f_e) but different initial jet opening half-angle ($\theta_0 = 0.1$ and 0.25 rad) and initial jet Lorentz factor ($\Gamma_0 = 100$ and 20) with $n_0 = 1.0$ cm^{-3} within $z = 0.05$. For our wide jet ($\Gamma_0 = 20$ and $\theta_0 = 0.1$ rad), the typical jet ($\Gamma_0 = 100$ and $\theta_0 = 0.1$ rad) and the jet with $\Gamma_0 = 20$ and $\theta_0 = 0.25$ rad, the peak of observed light curves at 0.3 TeV is at $t_{\rm peak,off} \sim 9.0\times10^4$ s, 3.0×10^5 s and 1.5×10^4 s, respectively (thick red solid, thin blue solid and thin green dashed lines in Fig. 9). The peak times for the three jets are different. If the light curve which has the observer time of the flux maximum at $t \sim 10^5$ s (thick red solid line in Fig. 9) is detected by CTA/4 LSTs with $n_0 = 1.0$ cm^{-3} within $z = 0.05$, we could confirm the existence of the wide jet.

5. Summary

In this paper, we have calculated afterglow emissions using the two-component jet model as given by Sato et al. (2021) to explain the new observational results of the VHE gamma-ray and radio bands (5.5 GHz and 99.8 GHz) of GRB 190829A. In our previous work (Sato et al., 2021), the number fraction of accelerated electrons was fixed as $f_e = 1.0$, while in this paper, we chosed $f_e = 0.2$ and 0.35 for the narrow and wide jets, respectively. As a result, our

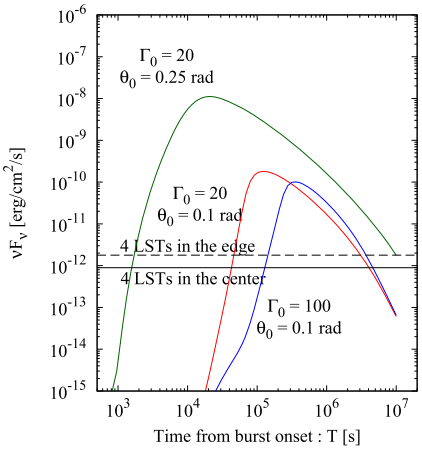

Fig. 9. VHE gamma-ray light curves at $h\nu = 0.3$ TeV. The value of θ_0 and Γ_0 is changed (thick red solid line: $\theta_0 = 0.1$ rad and $\Gamma_0 = 20$, thin blue dashed line: $\theta_0 = 0.1$ rad and $\Gamma_0 = 100$, thin green solid line: $\theta_0 = 0.25$ rad and $\Gamma_0 = 20$). We fix $z = 0.05$, $n_0 = 1.0$ cm^{-3}, $\theta_v = 0.3$ rad, $E_{\rm iso,K} = 1.0\times10^{53}$ erg, $\epsilon_B = 1.0\times10^{-5}$, $\epsilon_e = 0.29$, and $f_e = 0.35$. Sensitivities of CTA/4 LSTs at the center (black solid line) and CTA/4 LSTs at the edge (black dashed line) of the field of view are shown assuming an exposure time of three hours.[3]

numerical results in 1.3 and 15.5 GHz bands have been improved. In this paper, the Klein-Nishina effect in calculating the SSC process has been considered, so that our numerical X-ray light curve better matched than the results of Sato et al. (2021). The multi-wavelength afterglows of GRB 190829A were well explained by our two-component jet model (Fig. 2). Furthermore, the afterglow emissions from our two-component jet were consistent with the observed data of GRBs 180720B, 190114C and 201216C. The two-component jet, with the narrow-fast ($\theta_0 = 0.015$ rad and $\Gamma_0 = 350$) and wide-slow ($\theta_0 = 0.1$ rad and $\Gamma_0 = 20$) jets, may be required to explain the multi-wavelength afterglows of the VHE gamma-ray events. According to our two-component jet model, the detection rate of orphan afterglows within $z = 0.5$ by CTA/4 LSTs was about 0.1 yr^{-1}.

Declaration of competing interest

The authors declare that they have no known competing financial interests or personal relationships that could have appeared to influence the work reported in this paper.

Data availability

Data will be made available on request.

Acknowledgments

We thank Shotaro Abe, Kento Aihara, Katsuaki Asano, Giancarlo Ghirlanda, Gabriel Ghisellini, Kazuaki Hashiyama, Shotaro Ide, Kunihito Ioka, Kyohei Kawaguchi, Shota Kisaka, Asuka Kuwata, Lara Nava, Koji Noda, Yoshihiro Okutani, Takayuki Saito, Takanori Sakamoto, Haruka Sakemi, Om Sharan Salafia, Kensyo Sei, Kazuyoshi Tanaka, Kenta Terauchi, and Kenji Toma for valuable comments. This research has made use of the CTA instrument response functions provided by the CTA Consortium and Observatory, see https://www.cta-observatory.org/science/cta-performance/ (version prod5 v0.1; Cherenkov Telescope Array Observatory and Cherenkov Telescope Array Consortium (2021)) for more details. We also thank the referee for his or her helpful comments to substantially improve the paper. This research was partially supported by JSPS KAKENHI Grant Nos. 22J20105 (YS), 20H01901 (KM), 20H05852 (KM), 19H01893 (YO), 21H04487 (YO) and 22H01251 (RY). SJT is

supported by the Sumitomo Foundation for basic science research projects (210629), Research Foundation for Opto-Science and Technology, and Aoyama Gakuin University Research Institute. The work of KM is supported by the NSF Grant No. AST-1908689, No. AST-2108466 and No. AST-2108467. YO is supported by Leading Initiative for Excellent Young Researchers, MEXT, Japan.

References

Acciari, V.A., et al., 2021. Astrophys. J. 908, 90.
Abdalla, H., et al., 2019. Nature 575, 464.
Ajello, M., et al., 2019. Astrophys. J. 878, 52.
Asano, K., Murase, K., Toma, K., 2020. Astrophys. J. 905, 105.
Bellm, E.C., et al., 2019. Publ. Astron. Soc. Pac. 131, 018002.
Beniamini, P., Duque, R., Daigne, F., Mochkovitch, R., 2020. Mon. Not. R. Astron. Soc. 492, 2847.
Bietenholz, M.F., Bartel, N., Argo, M., Dua, R., Ryder, S., Soderberg, A., 2021. Astrophys. J. 908, 75.
Blanch, O., et al., 2020a. Gov. Comput. News 28659, 1.
Blanch, O., et al., 2020b. In: ATel, vol. 14275, p. 1.
Blumenthal, G.R., Gould, R.J., 1970. Rev. Mod. Phys. 42, 237.
Chand, V., et al., 2020. Astrophys. J. 898, 42.
Chen, Z., Sming Tsai, Y.-L., Yuan, Q.. J. Cosmol. Astropart. Phys. 2021, 025.
Cherenkov Telescope Array Consortium, et al., 2019. Science with the Cherenkov Telescope Array. World Scientific Publishing Co. Pte. Ltd.
Cherenkov Telescope Array Observatory and Cherenkov Telescope Array Consortium, 2021. CTAO instrument response functions - prod5 version v0.1, Zenodo. https://doi.org/10.5281/zenodo.5499840.
Derishev, E., Piran, T., 2019. Astrophys. J. Lett. 880, L27.
Derishev, E., Piran, T., 2021. Astrophys. J. 923, 135.
Dichiara, S., et al., 2022. Mon. Not. R. Astron. Soc. 512, 2337.
Donaghy, T.Q., 2006. Astrophys. J. 645, 436.
Duan, M.-Y., Wang, X.-G., 2019. Astrophys. J. 884, 61.
Duque, R., Beniamini, P., Daigne, F., Mochkovitch, R., 2022. Mon. Not. R. Astron. Soc. 513, 951.
Eichler, D., Waxman, E., 2005. Astrophys. J. 627, 861.
Evans, P.A., et al., 2007. Astron. Astrophys. 469, 379.
Evans, P.A., et al., 2009. Mon. Not. R. Astron. Soc. 397, 1177.
Fraija, N., Barniol Duran, R., Dichiara, S., Beniamini, P., 2019a. Astrophys. J. 883, 162.
Fraija, N., et al., 2019b. Astrophys. J. 885, 29.
Fraija, N., Dichiara, S., Pedreira, A.C.C. do E.S., Galvan-Gamez, A., Becerra, R.L., Barniol Duran, R., Zhang, B.B., 2019c. Astrophys. J. Lett. 879, L26.
Fraija, N., Veres, P., Beniamini, P., Galvan-Gamez, A., Metzger, B.D., Barniol Duran, R., Becerra, R.L., 2021. Astrophys. J. 918, 12.
Franceschini, A., Rodighiero, G., Vaccari, M., 2008. Astron. Astrophys. 487, 837.
Gao, H., Lei, W.-H., Zou, Y.-C., Wu, X.-F., Zhang, B., 2013. New Astron. Rev. 57, 141.
Gao, H.-X., et al., 2022. Preprint. arXiv:2204.03823.
Ghisellini, G., Tavecchio, F., Chiaberge, M., 2005. Astron. Astrophys. 432, 401.
Gottlieb, O., Bromberg, O., Singh, C.B., Nakar, E., 2020. Mon. Not. R. Astron. Soc. 498, 3320.
Granot, J., Piran, T., Sari, R., 1999. Astrophys. J. 513, 679.
Graziani, C., Lamb, D.Q., Donaghy, T.Q., 2006. AIPC News 836, 117.
H.E.S.S. Collaboration, 2021. Science 372, 1081.
Ho, A.Y.Q., et al., 2020. Astrophys. J. 905, 98.
Ho, A.Y.Q., et al., 2022. Preprint. arXiv:2201.12366.
Hu, Y.-D., et al., 2021. Astron. Astrophys. 646, A50.
Huang, Y.F., Gou, L.J., Dai, Z.G., Lu, T., 2000. Astrophys. J. 543, 90.
Huang, X.-L., Wang, Z.-R., Liu, R.-Y., Wang, X.-Y., Liang, E.-W., 2021. Astrophys. J. 908, 225.
Huang, Y.-J., et al., 2020. Astrophys. J. 897, 69.
Huang, Y., 2022. Preprint. arXiv:2204.08208.
Ioka, K., Nakamura, T., 2001. Astrophys. J. Lett. 554, L163.
Ivezić, Ž., et al., 2019. Astrophys. J. 873, 111.
Jacovich, T.E., Beniamini, P., van der Horst, A.J., 2021. Mon. Not. R. Astron. Soc. 504, 528.
Jordana-Mitjans, N., et al., 2020. Astrophys. J. 892, 97.
Kuwata, A., Toma, K., Kimura, S.S., Tomita, S., Shimoda, J., 2022. Preprint. arXiv:2208.09242.
MAGIC Collaboration, 2019a. Nature 575, 455.
MAGIC Collaboration, 2019b. Nature 575, 459.
Merloni, A., 2012. Preprint. arXiv:1209.3114.
Meszaros, P., Rees, M.J., 1993. Astrophys. J. 405, 278.
Mészáros, P., Rees, M.J., 1997. Astrophys. J. 476, 232.
Miceli, D., Nava, L., 2022. Galaxies 10, 66.
Murase, K., Toma, K., Yamazaki, R., Nagataki, S., Ioka, K., 2010. Mon. Not. R. Astron. Soc. 402, L54.
Murase, K., Toma, K., Yamazaki, R., Mészáros, P., 2011. Astrophys. J. 732, 77.
Nakar, E., Piran, T., Granot, J., 2002. Astrophys. J. 579, 699.
Nakar, E., Ando, S., Sari, R., 2009. Astrophys. J. 703, 675.
Nava, L., Sironi, L., Ghisellini, G., Celotti, A., Ghirlanda, G., 2013. Mon. Not. R. Astron. Soc. 433, 2107.
Pe'er, A., 2015. Adv. Astron. 2015, 907321.
Piran, T., 1999. Phronesis 314, 575.
Piran, T., 2004. Rev. Mod. Phys. 76, 1143.
Ravasio, M.E., et al., 2019. Astron. Astrophys. 626, A12.
Rhodes, L., et al., 2020. Mon. Not. R. Astron. Soc. 496, 3326.
Rhodes, L., van der Horst, A.J., Fender, R., Aguilera-Dena, D.R., Bright, J.S., Vergani, S., Williams, D.R.A., 2022. Mon. Not. R. Astron. Soc. 513, 1895.
Ronchi, M., 2020. Astron. Astrophys. 636, A55.
Rossi, E.M., Lazzati, D., Salmonson, J.D., Ghisellini, G., 2004. Mon. Not. R. Astron. Soc. 354, 86.
Sahu, S., Fortín, C.E.L., 2020. Astrophys. J. Lett. 895, L41.
Sahu, S., Valadez Polanco, I.A., Rajpoot, S., 2022. Astrophys. J. 929, 70.
Salafia, O.S., et al., 2022. Astrophys. J. Lett. 931, L19.
Sari, R., Piran, T., Narayan, R., 1998. Astrophys. J. Lett. 497, L17.
Sari, R., 1997. Astrophys. J. Lett. 489, L37.
Sari, R., Esin, A.A., 2001. Astrophys. J. 548, 787.
Sato, Y., Obayashi, K., Yamazaki, R., Murase, K., Ohira, Y., 2021. Mon. Not. R. Astron. Soc. 504, 5647.
Selina, R.J., et al., 2018. SPIE 10700, 107001O.
Shimoda, J., Toma, K., 2021. Astrophys. J. 913, 58.
Shrestha, M., 2022. Preprint. arXiv:2208.01729.
Totani, T., Panaitescu, A., 2002. Astrophys. J. 576, 120.
Urata, Y., Huang, K., Yamazaki, R., Sakamoto, T., 2015. Astrophys. J. 806, 222.
Urrutia, G., De Colle, F., López-Cámara, D., 2022. Preprint. arXiv:2207.07925.
Valeev, A.F., et al., 2019. In: ATel, vol. 25565, p. 1.
Wang, X.-Y., He, H.-N., Li, Z., Wu, X.-F., Dai, Z.-G., 2010. Astrophys. J. 712, 1232.
Wang, X.-Y., Liu, R.-Y., Zhang, H.-M., Xi, S.-Q., Zhang, B., 2019. Astrophys. J. 884, 117.
Yamasaki, S., Piran, T., 2022. Mon. Not. R. Astron. Soc. 512, 2142.
Yamazaki, R., Ioka, K., Nakamura, T., 2002. Astrophys. J. Lett. 571, L31.
Yamazaki, R., Ioka, K., Nakamura, T., 2003a. Astrophys. J. 593, 941.
Yamazaki, R., Yonetoku, D., Nakamura, T., 2003b. Astrophys. J. Lett. 594, L79.
Yamazaki, R., Ioka, K., Nakamura, T., 2004. Astrophys. J. Lett. 606, L33.
Yamazaki, R., Sato, Y., Sakamoto, T., Serino, M., 2020. Mon. Not. R. Astron. Soc. 494, 5259.
Zhang, B., 2018. The Physics of Gamma-Ray Bursts. Cambridge Univ. Press, Cambridge.
Zhang, B.T., Murase, K., Veres, P., Mészáros, P., 2021b. Astrophys. J. 920, 55.
Zhang, L.-L., Ren, J., Huang, X.-L., Liang, Y.-F., Lin, D.-B., Liang, E.-W., 2021a. Astrophys. J. 917, 95.
Zhang, W., MacFadyen, A., 2009. Astrophys. J. 698, 1261.